Interplay between stimulated Brillouin scattering and Kerr filamentation with an inertial plasma response

Jérémie Rolle and Luc Bergé
CEA, DAM, DIF, 91297 Arpajon, France
(Received 28 March 2014; published 28 May 2014)

The filamentation of ultraviolet and infrared nanosecond light pulses in fused silica is investigated theoretically and numerically. Emphasis is put on the action of a dynamical plasma response on two counterpropagating waves, amplified by Kerr self-focusing and stimulated Brillouin scattering (SBS). For a single unperturbed wave, laser filamentation takes place through a quasistationary balance between Kerr self-focusing and plasma defocusing, for which a variational approach reproduces global propagation features. However, such a quasistationary balance cannot hold as temporal modulational instability breaks up the pulse over electron recombination times. For two counterpropagating waves, we report similar instabilities which are justified through a plane-wave stability analysis. These instabilities originate from an intense backscattered wave that induces strong plasma contribution and thus destabilizes the pump near the entrance face of the material. Rapid phase modulations are then applied to suppress backscattering. We show that pump waves with broad enough bandwidths can inhibit SBS and thus prevent instability. The robustness of phase modulations against random fluctuations in the input pump pulse is finally addressed.

DOI: 10.1103/PhysRevA.89.053834 PACS number(s): 42.65.Jx, 72.20.Jv, 79.20.Ws

I. INTRODUCTION

Stimulated Brillouin scattering (SBS) occurs in a large variety of optical settings, such as silica devices employed in high-power laser systems [1,2], optical fibers [3], or nanostructured materials [4]. It also plays a key role in the scopes of stimulated Rayleigh-Bragg scattering [5], optical storing [6], and slow light propagation [7–9].

SBS is initiated by the electrostriction strain driven by a long and intense laser pulse in optically transparent media having no linear absorption. This strain exerts a ponderomotive force, that initiates acoustic waves on which Stokes waves backscatter part of laser energy. Because the Stokes wave increases with an exponential growth, it can damage the front surface of the sample at high input powers [10,11]. Discovered in the 1960s, SBS has been abundantly investigated [12–14], but rarely in the presence of Kerr self-focusing. Addressed in [15–17], pump pulses with broad enough bandwidth were numerically demonstrated to suppress SBS in regimes where they self-focus toward intensities of a few TW/cm^2. At such high intensities, saturation of the Kerr self-focusing by a plasma response becomes important. In [16,17], a stationary plasma model inspired from Ref. [18] was used, i.e., plasma just acted as an instantaneous higher-order nonlinearity [19]. This model was tested with heavy numerics performed on graphical processors, which showed that nanosecond optical waves could currently attain 6–8 TW/cm^2 with a noninertial (stationary) plasma response [20].

Some work, however, devoted to nanosecond filaments supported by an inertial plasma in gases [21], outlined that self-channeling long pulses could suffer modulational instabilities, leading to pulse breakup in time and collapse events over picosecond durations. For many practical applications, the nonlinear propagation of long pulses in $(3+1)$-dimensional bulk materials involving Kerr, Brillouin, and ionization effects are highly relevant. In particular, sharp instabilities can deeply affect nanosecond pulses and cause premature damage in the optics of large-scale laser facilities. Plasma generation then becomes a challenging issue, as optical damage starts once ionization intensity thresholds have been exceeded. To reduce backscattering and related damage at the front face of dielectrics, broadband pump pulses can be exploited [22–24]. An important point is thus to know whether phase modulations keep their efficiency with plasma generation.

To answer this question, we investigate the propagation of intense light pulses with duration close to 1 ns at full width at half maximum (FWHM) in fused silica. We shall first demonstrate that single, *initially unperturbed* nanosecond pulses can remain robust over a few cm of filamentation and support a stationary plasma, whose action can be deduced from a variational model. Once this propagation range has been crossed through, short-time instabilities destroy the pulse profile in time in a way similar to Ref. [21]. Such instabilities are attributed to the dynamical plasma response. They are found to take place over the electron recombination time $\sim$150 fs, which is supported by a plane-wave stability analysis. Second, our investigation will include an SBS-created Stokes wave. We report strong plasma generated by intense Stokes components near the entrance face of the material, which again yields pump instabilities over electron recombination times. Third, phase modulations are tested to suppress Brillouin backscattering with an inertial plasma. We show that pump pulses with broad enough bandwidth can delete both Brillouin scattering and plasma-driven instabilities. The efficiency of phase modulations is finally tested with respect to a random noise in the laser pump pulse. We demonstrate that random fluctuations do unfortunately affect phase modulation efficiency.

This paper is organized as follows. Section II recalls the model equations describing the competition between Kerr self-focusing, stimulated Brillouin scattering, and ionization. Section III discusses the propagation of a single nanosecond wave operating at 355 nm, whose dynamics are explained by a variational approach and plane-wave stability analysis. Section IV presents theoretical and numerical results, when

 ©2014 American Physical Society

both pump and Stokes waves trigger plasma in silica. Emphasis is put on instability patterns upon short time scales. Section V deals with the action of phase modulations on the pump wave to suppress Brillouin effect. Section VI addresses similar features at 1064 nm pump wavelength. Section VII revisits the effect of phase modulations for noisy inputs.

II. MODEL EQUATIONS

For pure silica with no optical loss, Stokes waves are scattered by laser-induced pressure gradients exerted in the bulk by electrostriction. Owing to self-focusing, both pump and Stokes waves can reach several TW/cm^2 in intensity and are thus able to ionize SiO_2 molecules. Our model equations take into account the interplay between the pump and Stokes waves, the phonon waves, and an electron plasma. The electric field, assumed to be linearly polarized, is a combination of two optical components:

$$E = \sqrt{c_1}(U_1 e^{ik_1 z - i\omega_1 t} + U_2 e^{-ik_2 z - i\omega_2 t} + \text{c.c.}), \tag{1}$$

where $c_1 \equiv \mu_0\omega_0/2k_0$ is a normalization factor and μ_0 is the magnetic permeability in vacuum (c.c. means complex conjugate). The slowly varying envelopes for the pump and Stokes waves, U_1 and U_2, respectively, have their center frequency close to $\omega_0 = 2\pi c/\lambda_0 = k_0 c/n_0$ (c is the speed of light in vacuum and n_0 is the linear index of silica at pump wavelength λ_0) and comparable group velocities, $k_1' \approx k_2' \approx k' \simeq n_0/c$ ($k_1 \approx k_2 \approx k_0$).

Following [10,11], the laser electric field is governed by the wave equation

$$\vec{\nabla}^2 E - c^{-2}\partial_t^2 E = \mu_0\left(\partial_t^2 P + \partial_t J\right). \tag{2}$$

Describing the bounded electron response of the material, P denotes the polarization vector

$$P = \epsilon_0\chi^{(1)}E + \epsilon_0\chi^{(3)}E^3 + \epsilon_0\Delta\epsilon E, \tag{3}$$

where the first component refers to linear polarization with first-order susceptibility tensor $\chi^{(1)}$, the second one is the nonlinear (Kerr) polarization with third-order susceptibility tensor $\chi^{(3)}$, and the last one originates from electrostriction [$\epsilon_0 = 1/\mu_0 c^2$]. $\Delta\epsilon = \gamma_e\Delta\rho/\rho_0$ refers to the variation in the dielectric constant produced by the density fluctuation $\Delta\rho$ through electrostriction. γ_e is the electrostriction coefficient and ρ_0 is the bulk material density. $\Delta\rho$ is governed by the acoustic wave equation

$$\left[\partial_t^2 - \Gamma'\vec{\nabla}^2\partial_t - C_s^2\vec{\nabla}^2\right]\Delta\rho = \vec{\nabla}\cdot\vec{f}_e, \tag{4}$$

and searched under the form

$$\Delta\rho \propto Q\, e^{i(qz-\omega_s t)} + \text{c.c.}, \tag{5}$$

with complex envelope function Q, wave number $q = 2k_1$ ($\vec{q} = \vec{k}_1 - \vec{k}_2$), and frequency $\omega_s = \omega_1 - \omega_2 \simeq C_s q$, where $C_s = 5.97\times10^5$ cm/s is the sound velocity. Γ' is the material damping parameter and $\vec{f}_e$ is the electrostriction strain such that $\vec{\nabla}\cdot\vec{f}_e = -(\gamma_e/2n_o c)\nabla^2 E^2$.

Equations for U_1, U_2, and Q are derived by substituting Eq. (1) into Eq. (2), and Eq. (5) into Eq. (4). We omit higher-order derivatives and phonon propagation [11], and discard harmonic generation in the Kerr contributions where only self- and cross-phase modulations with nonlinear index $n_2 \equiv 3\mu_0 c\chi^{(3)}/4n_0^2$ are retained. Following [25], the phonon waves are seeded by a thermal Gaussian random noise, $\tilde{N}$, with zero mean and such that

$$\langle\tilde{N}(\vec{r},t)\tilde{N}^*(\vec{r}',t')\rangle = A_{\tilde{N}}\delta(\vec{r}-\vec{r}')\delta(t-t'), \tag{6}$$

where $A_{\tilde{N}} \simeq 3.7\times10^{-29}$ GW^2 ns/cm at 300 K (symbol * means c.c.).

We also incorporate the effect of plasma generation through the term $\mu_0\partial_t J$ in Eq. (2). The scalar current density is given by $J = q_e\rho v_e$, where q_e is the electron charge, ρ is the free electron density, and v_e is their velocity. We use a simple Drude model for the electron velocity, yielding $\partial_t J \simeq q_e^2\rho E/m_e$. The source equation for ρ is modeled as [26–30]

$$\frac{\partial\rho}{\partial t} = W(I)\rho_{\text{nt}} - \frac{\rho}{\tau_{\text{rec}}}, \tag{7}$$

involving the total field intensity I. Here, $\rho_{\text{nt}} = 2.2\times10^{22}$ cm^{-3} is the density of neutral species, τ_{rec} is the recombination time of electrons in silica, and $W(I)$ is the photoionization rate. We assume $\rho \ll \rho_{\text{nt}}$ and neglect avalanche ionization. We numerically verified that, over a few cm, plasma generation remains mainly driven by the photoionization process. The ionization rate $W(I)$ is evaluated in the multiphoton limit $W(I) = \sigma_K I^K$, where σ_K is the associated cross section [31]. $K = \text{mod}(U_i/\hbar\omega_0) + 1$ is the minimum number of photons with energy $\hbar\omega_0$ necessary to extract an electron from neutral species with ionization energy U_i. We select the gap potential $U_i = 9$ eV, while the electron recombination time is $\tau_{\text{rec}} = 150$ fs [32]. Losses induced by photoionization are evaluated from Poynting's theorem leading to

$$\mu_0\frac{\partial J_{\text{loss}}^{\text{PI}}}{\partial t} = -ik_0\beta^{(K)}I^{K-1}E, \tag{8}$$

where $\beta^{(K)} = \sigma_K K\hbar\omega_0\rho_{\text{nt}}$ is the multiphoton absorption (MPA) coefficient.

So far in SBS context [20], the plasma response has been assumed stationary, i.e.,

$$\rho(t) \simeq \tau_{\text{rec}}\rho_{\text{nt}}\sigma_K I^K. \tag{9}$$

In the present work, we examine, instead, the effect of a dynamical (inertial) plasma response. For technical convenience, we assume that at each point of space (x,y,z,t) the forward wave intensity $I_1 \equiv |U_1|^2$ is large when the Stokes intensity $I_2 \equiv |U_2|^2$ is relatively small, in such a way that $I \simeq I_1 + I_2$ and $I^K \simeq I_1^K + I_2^K$. By comparison with Refs. [16,20], our plasma response appears simplified under the previous assumption. We checked, however, that the peak intensities and maximum electron densities are similar when using the full stationary plasma model of [16] or that one assuming $I^K \simeq I_1^K + I_2^K$.

Under the latter simplification, we finally obtain the set of equations governing the interplay between Kerr self-focusing, SBS, and plasma generation:

$$(\partial_z + k'\partial_t)U_1 = \frac{i\nabla_\perp^2 U_1}{2k_0} + i\frac{\omega_0}{c}n_2(I_1+2I_2)U_1 - \frac{g_0}{2}QU_2 - i\frac{k_0}{2n_0^2\rho_c}\rho U_1 - \frac{\beta^{(K)}}{2}I_1^{K-1}U_1, \tag{10}$$

TABLE I. Physical parameters for silica at 355 nm and 1064 nm.

Physical parameters	$\lambda_0 = 355$ nm	$\lambda_0 = 1064$ nm
n_0	1.4762	1.454
P_{cr} [MW]	0.377	4.59
n_2 [cm^2/W]	3.6×10^{-16}	2.7×10^{-16}
τ_B [ns]	1.1	10
K	3	8
σ_K [ns^{-1} cm^{2K}/GW^K]	2.46×10^{-11}	8.36×10^{-33}
ρ_c [cm^{-3}]	8.8×10^{21}	9.8×10^{20}
$\beta^{(K)}$ [cm^{2K-3}/GW^{K-1}]	9.16×10^{-7}	2.75×10^{-28}

$$(-\partial_z + k'\partial_t)U_2 = \frac{i\nabla_\perp^2 U_2}{2k_0} + i\frac{\omega_0}{c}n_2(I_2 + 2I_1)U_2 + \frac{g_0}{2}Q^*U_1 - i\frac{k_0}{2n_0^2\rho_c}\rho U_2 - \frac{\beta^{(K)}}{2}I_2^{K-1}U_2, \quad (11)$$

$$\tau_B\partial_t Q + Q = U_1U_2^*, \quad (12)$$

$$\partial_t\rho = \sigma_K\rho_{nt}\left(I_1^K + I_2^K\right) - \frac{\rho}{\tau_{rec}}, \quad (13)$$

where z is the propagation variable and $\nabla_\perp^2 = \partial_x^2 + \partial_y^2$ is the diffraction operator in the (x,y) plane. $g_0 \simeq 5$ cm/GW is the Brillouin gain factor evaluated for the bulk silica density $\rho_0 = 2.21$ g/cm^3 [3,11,33]. $\tau_B = 2/\Gamma_B = 2/q^2\Gamma'$ is the phonon damping rate, where Γ_B is the Brillouin linewidth related to the gain spectral bandwidth $\Delta\nu_B = \Gamma_B/2\pi$. Numerical values for our relevant physical parameters are given in Table I.

Equations (10)–(13) are integrated in full 3D geometry, for an input pump pulse with spatial Gaussian profile and a temporal profile being super-Gaussian,

$$U_1(z=0) = \sqrt{I_1(0)}e^{-(x^2+y^2)/w_0^2 - t^{2N}/t_p^{2N}}, \quad (14)$$

of order $N = 2$, with $1/e^2$ initial beam width w_0 and half-length $t_p = 0.5$ ns. The input pump intensity $I_1(0)$ is linked to the peak power $P_1(0)$ through the relation $I_1(0) = 2P_1(0)/\pi w_0^2$. $P_1(0)$ will be expressed in terms of the critical power for self-focusing, $P_{cr} \simeq \lambda_0^2/(2\pi n_0 n_2)$.

Using laser pulses with FWHM durations of 0.77 ns, the product $\Gamma_B t_p$ is of order unity. In that case, SBS develops in transient regime [10,11], for which the nonstationary exponential gain of the Stokes intensity is mainly given for an undepleted plane-wave pump [12,22] by

$$G_T(z) \sim 2\sqrt{\Gamma_B t_p g_0 I_1(0)(L-z)}, \quad (15)$$

i.e., $I_2(0)/I_2(L) \sim \exp G_T(0)$.

Besides Brillouin backscattering, the Kerr response can lead to wave collapse at powers $P_i \equiv \int I_i d\vec{r}_\perp \geqslant P_{cr}$ [34,35]. For an unperturbed Gaussian pump, the collapse distance can be estimated by Marburger's formula [36]

$$z_c \simeq L_M = \frac{0.367 z_0}{[(\sqrt{P_1/P_{cr}} - 0.852)^2 - 0.0219]^{1/2}}, \quad (16)$$

where $z_0 = \pi n_0 w_0^2/\lambda_0$ is the Rayleigh length. To integrate our model equations (10)–(13), we shall use a split-step parallel code, namely, the "SBS-3D" code detailed in [20], employing longitudinal and temporal grid spacings linked by $\Delta z = \Delta t/k'$. Integration in the (x,y) plane is performed by means of fast Fourier transforms. The main constraint being the volume of the numerical box versus the computation time, we limit the *maximum* number of points to $256 \times 256 \times 16\,384$ points in (x,y,z). Minimum transverse steps are fixed to $\Delta x = \Delta y = 0.94$ μm, while Δz and Δt may vary in the intervals $0.1 \leqslant \Delta z \leqslant 2$ μm and $0.75 \leqslant \Delta t \leqslant 10$ fs, depending on the sample thickness. Coarser (z,t) steps can limit the description of the plasma response. However, they are at least three times smaller than those achieved in [20] on graphical processors. Generally, the heavy meshes used in our full 3D SBS simulations ($\Delta t \leqslant 10$ fs for a time window of 3 ns) will force us to limit the graphical resolution of our surface plots to ~6–7.5 ps.

III. ONE-WAVE DYNAMICS

We here examine the nonlinear propagation of a *single* nanosecond pulse in silica, in order to benchmark the plasma response at UV wavelength $\lambda_0 = 355$ nm. Before testing the SBS code in this configuration, we perform computations from a second code integrating the forward-Maxwell equation (FME) (see Refs. [37,38]). This code uses a Cranck-Nicholson scheme over the radius $r_\perp = \sqrt{x^2+y^2}$. It has an adaptive step along z and can account for many additional physical effects, such as higher-order dispersion, self-steepening [39], and avalanche ionization [40,41]. Constrained to the radial symmetry, this code is able to maintain longitudinal and temporal steps to their lowest bounds, namely, $\Delta z \approx 0.1$ μm and $\Delta t < 1$ fs, while keeping the same transverse resolution as above.

A. Quasistationary regime

Figures 1(a) and 1(b) show the maximum intensity and peak electron density attained with $w_0 = 60$ μm and $P_1(0) = 4P_{cr}$ [$I_1(0) = 26.7$ GW/cm^2] when using the FME code. For initially unperturbed pulses, the maximum intensity reaches a plateau clamped at $I_{max} \simeq 7$ TW/cm^2 and the peak electron density reaches $\rho_{max} \simeq 3 \times 10^{19}$ cm^{-3} as long as $z \leqslant 2.7$ cm. In this range the pulse forms a quasistable filament clamped at the peak values [38]

$$I_{max} \approx \left(\frac{2n_0 n_2 \rho_c}{\Delta\tau\sigma_K\rho_{nt}}\right)^{1/(K-1)}, \quad \rho_{max} \approx \Delta\tau\sigma_K I_{max}^K\rho_{nt}, \quad (17)$$

when one assumes that plasma continuously accumulates over, e.g., $\Delta\tau = 1$ ps. In Figs. 1(a) and 1(b), the pulse undergoes this clamping mechanism until an instability takes place from $z > 2.7$ cm. This instability manifests by a noticeable increase of the peak density and of the optical intensity beyond 10 TW/cm^2. Such intensity levels agree with Eq. (17) when one assumes an efficient defocusing over the electron recombination time $\Delta\tau = 150$ fs.

Figure 1(c) illustrates the on-axis pulse dynamic in the (z,t) plane. In self-channeling regime, an unperturbed pulse self-focuses not only in z, but also in time, along which the pulse splits into parabolas resulting from the balance between transverse diffraction, Kerr self-focusing, and plasma defocusing. This dynamic does not change when introducing chromatic dispersion, i.e., group-velocity dispersion (GVD) with coefficient $k'' = 1169$ fs^2/cm and third-order dispersion

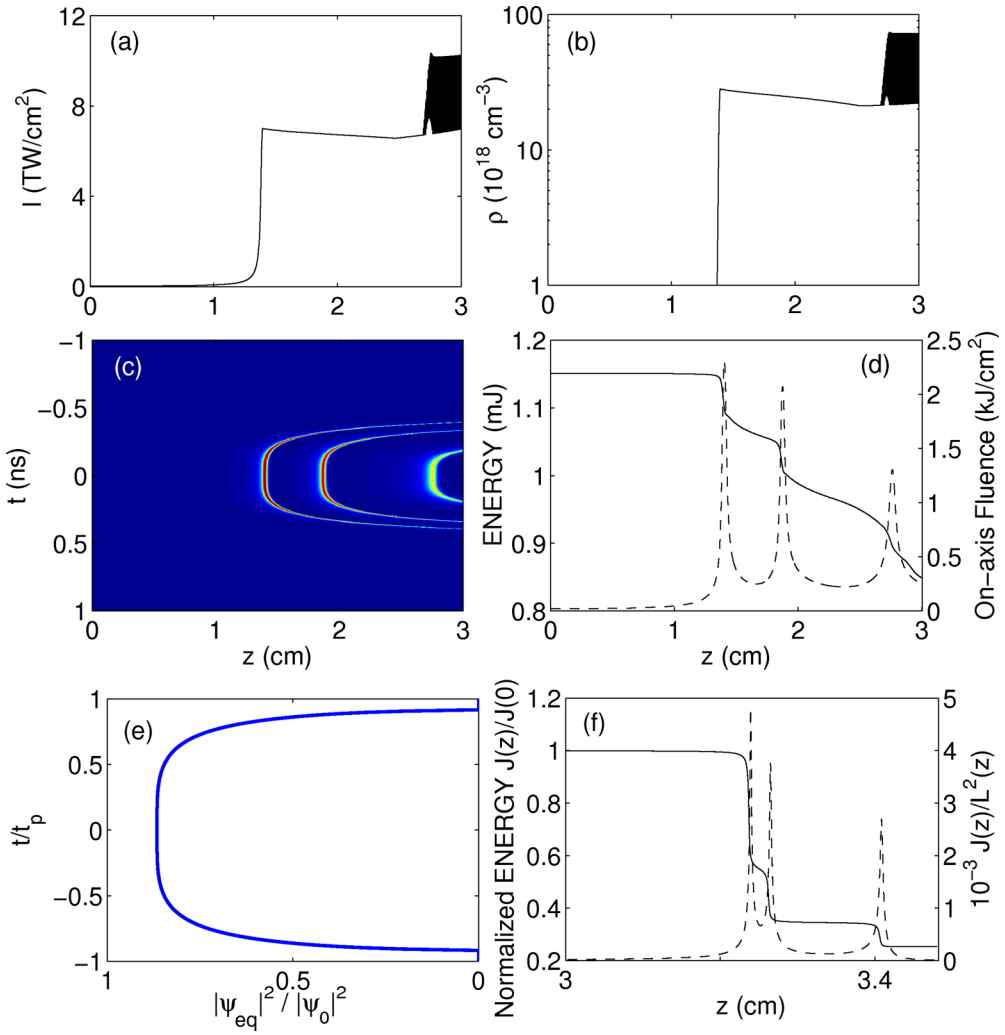

FIG. 1. (Color online) Self-guiding of a 0.77 ns FWHM, 60-μm, 355-nm pulse in silica computed from an unidirectional pulse propagation model (FME). (a) Maximum intensity, (b) peak electron density, (c) pulse on-axis dynamic in the (z,t) plane, and (d) evolution of energy (solid curve, left axis) and on-axis fluence (dashed curve, right axis) along z. (e) Plot of $|\psi_{eq}/\psi_0|^2$ for $P_{in}/P_{cr} = 4$. (f) Variational energy losses $J(z)/J(0)$ and intensity, $J(z)/L^2(z)$, for the same pulse. For (e),(f), results are obtained from the numerical solving of Eqs. (19) and (20).

(TOD) with coefficient $k''' = 348$ fs^3/cm at 355 nm [42], also able to cause pulse splitting in time [43]. At maximum intensity, the pulse attains its highest fluence values (>1 kJ/cm^2) [Fig. 1(d)], as long as the integrity of the pulse profile is preserved. At $t = 0$, three focii occur along $z \leqslant 3$ cm, through which the pulse, compressed to the filament diameter $\phi_p \simeq 2.5$ μm, triggers ionization and loses part of its power.

The previous behaviors can be explained from a variational approach [44–47]. In particular, the temporal pattern of Fig. 1(c) is the signature of a quasistationary equilibrium between Kerr self-focusing and plasma generation. Indeed, using rescaled variables $r \to w_0 r$, $z \to 4z_0 z$, and $t \to t_p t$, let us assume that U_1 collapses self-similarly with the transverse width $L(z,t)$ near the finite blowup distance z_c [34,48–50]. U_1 behaves as $|U_1| \to |\psi(z,r,t)| = \sqrt{J(z,t)}R(r/L)/L$, where $J(z,t)$ accounts for the power losses due to dissipation such as

$$J(z=0,t) = \frac{P_{in}}{P_{cr}} e^{-2t^{2N}}, \quad P_{in} \equiv P_1(0), \tag{18}$$

and R is the Townes profile. Straightforward calculations yield the dynamical system (see Ref. [47] for more detail)

$$\frac{M}{4P_c} L^3 \partial_z^2 L = 1 - J + C\frac{J^K}{L^{2(K-1)}}, \tag{19}$$

$$\partial_z \ln J \simeq -2\nu A \frac{J^{K-1}}{L^{2(K-1)}}. \tag{20}$$

M, C, and A are positive integral coefficients, $P_c \equiv \int R^2 d\vec{\xi} \simeq 11.7$ with $\vec{\xi} \equiv \vec{r}_\perp/L(z,t)$ is the dimensionless collapse threshold, and we have supposed a stationary plasma, $\rho = \Gamma|\psi|^{2K}$ where $\Gamma = \text{const}$. The first equation reflects the vanishing of $L(z,t)$ when pulse power is supercritical. The second equation reflects losses induced by MPA.

Neglecting MPA losses, it is straightforward to establish from Eq. (19) the potential-well formulation

$$E(z,t) = \frac{1}{2}\left[\frac{\partial L}{\partial z}\right]^2 + \Pi(L) = E(0,t), \tag{21}$$

$$\Pi(L) = \left(\frac{1-J}{L^2} + \frac{CJ^K}{KL^{2K}}\right)\frac{2P_c}{M}. \tag{22}$$

The potential $\Pi(L)$ possesses a global minimum only when $J(0,t) > 1$, i.e., when $P_{\rm in} > P_{\rm cr}$ and t belongs to the physical time interval $-t_* < t < t_*$, where $t_* = (\ln\sqrt{P_{\rm in}/P_{\rm cr}})^{1/2N} t_p$. This minimum is attained at the equilibrium beam width $L \equiv L_{\rm eq}$ that solves $\frac{d}{dL}\Pi(L) = 0$, thereby yielding

$$\frac{|\psi_{\rm eq}|^2}{|\psi_0|^2} = \left[1 - \frac{P_{\rm cr}}{P_{\rm in}} e^{t^{2N}}\right]^{1/(K-1)}, \tag{23}$$

where ψ_0 denotes a convenient normalization constant. Equation (23) indicates that the balance between diffraction, Kerr focusing and multiphoton ionization takes place along parabolas in time, resulting in symmetric pulse splitting. Figure 1(e) *quantitatively* reproduces this phenomenon for $K = 3$. The location of the focused pulse in time domain explains the (z,t) pattern of Fig. 1(c). With four critical powers and $t_p = 0.5$ ns, the equilibrium between self-focusing and plasma generation is localized at times $t < t_* = 0.92 \times t_p \simeq 0.46$ ns, which indeed agrees with Fig. 1(c).

Once the first focusing event is passed, the pump undergoes energy loss through MPA. We expect that, at the distance where this event takes place, the pulse power exhibits a stepwise decrease ($J_z \propto -L^{2-2K}$) corresponding to the rapid vanishing of $L(z,t)$ near $z = z_c \simeq 1.4$ cm.

With $P_{\rm in} = 4P_{\rm cr}$, more focusing-defocusing cycles develop. Figure 1(d) shows energy losses and on-axis fluences [$\mathcal{F}(\vec{r}) \equiv \int I(\vec{r},t)dt$] along the propagation distance z. We observe the expected stepwise decrease of the pulse energy at each cycle balancing Kerr self-focusing and plasma generation. For comparison, Fig. 1(f) presents the same pieces of information inferred from the dynamical variational equations (19) and (20) at $t = 0$. Results reproduce the three stepwise decreases of energy linked to the three focusing-defocusing cycles. Note that the self-focusing distances and amount of energy losses quantitatively differ from those obtained from direct numerics. Discrepancies are due to standard limitations of the variational model, which always keeps a Gaussian profile in space and preserves a super-Gaussian profile in time. Nonetheless, the global propagation features in the nanosecond regime are well reproduced by this variational method.

B. Plasma instabilities

From Figs. 1(a) and 1(b), we can observe that, over long enough propagation distances in self-channeling regime, the pulse intensity leaves the plateau $I_{\rm max} \sim 7\,{\rm TW/cm^2}$ to increase toward higher values. To understand this behavior, we develop a stability analysis comparable to that performed in [21,51]. Returning to physical variables, we discard MPA losses and consider a zeroth-order plane-wave solution $U_s = \phi\, e^{i\Lambda z}$ corresponding to the stationary density $\rho_s = \tau_{\rm rec}\sigma_K \rho_{\rm nt} I_s^K$ ($I_s \equiv |\phi|^2$), yielding

$$\Lambda = \frac{n_2\omega_0}{c} I_s - \alpha I_s^K, \quad \alpha \equiv \frac{k_0 \tau_{\rm rec}\rho_{\rm nt}\sigma_K}{2n_0^2\rho_c}. \tag{24}$$

We then introduce the perturbed state [$\vec{r}_\perp \equiv (x,y)$]:

$$U(\vec{r}_\perp,z,t) = U_s(\vec{r}_\perp,z) + \tilde{u}^+(\vec{r}_\perp,z)e^{-i\Omega t} + \tilde{u}^-(\vec{r}_\perp,z)e^{i\Omega t}, \tag{25}$$

where the frequency Ω is assumed real and $|\tilde{u}^+,\tilde{u}^-| \ll |U_s|$. Accordingly, we set

$$\rho(\vec{r}_\perp,z,t) = \rho_s(\vec{r}_\perp,z) + \rho^+(\vec{r}_\perp,z)e^{-i\Omega t} + \rho^-(\vec{r}_\perp,z)e^{i\Omega t}, \tag{26}$$

where $\rho^- = \bar{\rho}^+$ (bar symbol means complex conjugate). It is then easy to deduce from Eq. (13)

$$\rho^+ = K\rho_{\rm nt}\sigma_K I_s^{K-1} \frac{(\tilde{u}^+\bar{U}_s + \bar{\tilde{u}}^- U_s)}{\tau_{\rm rec}^{-1} - i\Omega}. \tag{27}$$

By linearizing Eq. (10) with $U_2 = 0$, we consider ϕ as real and look for perturbations in the form $\tilde{u}^\pm = u^\pm e^{i\Lambda z}$, where $u^\pm$ oscillates in the transverse plane with wave vector $\vec{k}_\perp$, i.e., $u^\pm \sim \cos(\vec{k}_\perp \cdot \vec{r}_\perp)$. Introducing $v = u^+ + \bar{u}^-$ and $w = u^+ - \bar{u}^-$, we then obtain

$$[\partial_z - ik'\Omega]v = -i\frac{k_\perp^2}{2k_0} w, \tag{28}$$

$$[\partial_z - ik'\Omega]w = i\left(2n_2\frac{\omega_0}{c} I_s - \frac{k_\perp^2}{2k_0} - \frac{2\alpha K I_s^K}{1 - i\Omega\tau_{\rm rec}}\right)v. \tag{29}$$

With $v,w \propto e^{\lambda z}$, combining Eqs. (28) and (29) yields

$$\lambda = {\rm Re}\left[\frac{k_\perp}{\sqrt{2k_0}}\sqrt{2\frac{\omega_0}{c}\left(n_2 I_s - \frac{K\rho_s}{2n_0\rho_c(1 - i\Omega\tau_{\rm rec})}\right) - \frac{k_\perp^2}{2k_0}}\right]. \tag{30}$$

This result is comparable to that derived by Niday *et al.* [21]. Figures 2(a) and 2(b) show two examples of growth rates λ in the $(k_\perp,\Omega)$ plane. For small intensity ($I_s = 0.5\,{\rm TW/cm^2}$) out of the self-guiding regime, plasma generation is negligible. Temporal fluctuations owing to the Ω dependence of the perturbation play no relevant role, and we just refind the standard growth rate $\lambda \sim k_\perp\sqrt{(2\omega_0 n_2/c)I_s - k_\perp^2/2k_0}$ for transverse modulational instabilities in a cubic medium [52,53]. In contrast, when the pulse intensity is close to its clamping value, $I_s \simeq 7\,{\rm TW/cm^2}$, the plasma response competes efficiently with Kerr focusing. The inertial nature of the free electron density manifests by an instability in time being maximum near $\Omega\tau_{\rm rec} \simeq 1$. This instability originates from the finite extent-in-time of the plasma response, which, by feedback, breaks up the pulse profile into short-scaled structures over the finite lifetime of the freed electrons ($\tau_{\rm rec} = 150$ fs). It occurs for large enough values of $k_\perp$, i.e., when the transverse beam width reaches the filament waist. Instability disappears in the limit $\Omega \to 0$, which corresponds to a stationary plasma. In time domain, such a short-scale instability only initiated by the numerical noise clearly appears in Fig. 2(c), where short spikes emerge over subpicosecond time scales due to the rapid defocusing action of the plasma [Fig. 2(d)]. Figure 2(e) displays the on-axis spectrum of the pulse evaluated at $z = 1.5$ cm, where the pulse preserves a narrow spectrum, and at $z = 2.84$ cm, where the pulse develops shorter peaks that give rise to a triangular spectral shape prolonged by a strong blueshift over the frequency variation $\Delta\omega \simeq 3.3 \times 10^{13}\ {\rm s^{-1}}$. As justified in [54], the triangular spectrum is a universal pattern that results from successive energy transfers between spectral components from the central mode to adjacent sidebands due

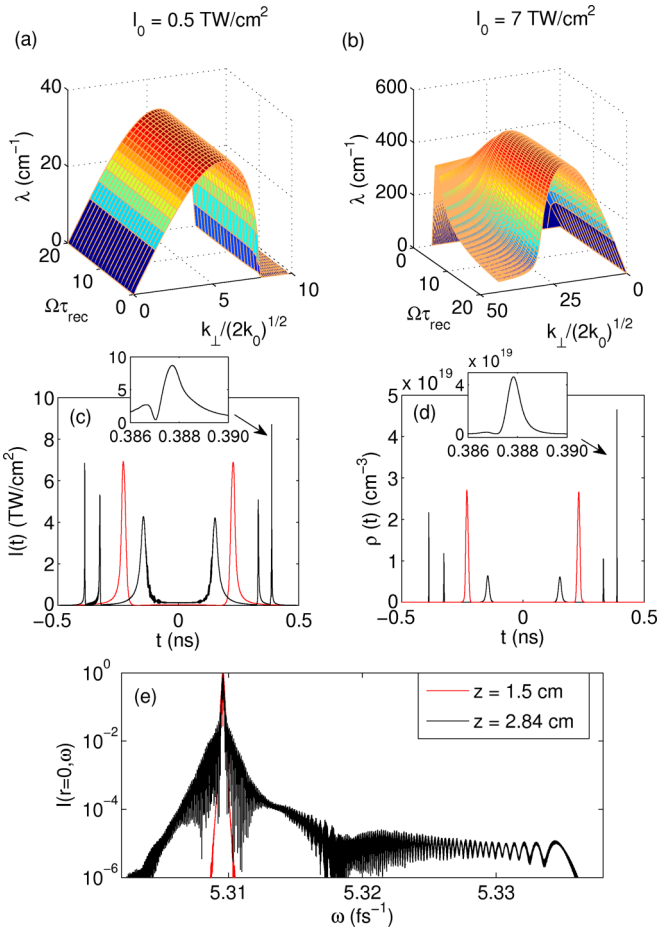

FIG. 2. (Color online) Contour plots of growth rate λ [cm^{-1}] in the plane $(k_\perp/\sqrt{2k_0}, \Omega\tau_{\rm rec})$ for $\lambda_0 = 355$ nm: (a) $I_s \equiv I_0 = 0.5$ TW/cm^2; (b) $I_s \equiv I_0 = 7$ TW/cm^2. (c) Maximum intensity along time for $z = 1.5$ cm (red [gray] curve) and $z = 2.84$ cm (black curve). The FWHM of the most intense peak is 800 fs (see inset). (d) Plasma density along time at the same distances. The most intense electron peak has a FWHM of ~650 fs (see inset). (e) On-axis normalized intensity spectra vs pulse frequency ω at $z = 1.5$ cm (red [gray] curve) and $z = 2.84$ cm (black curve).

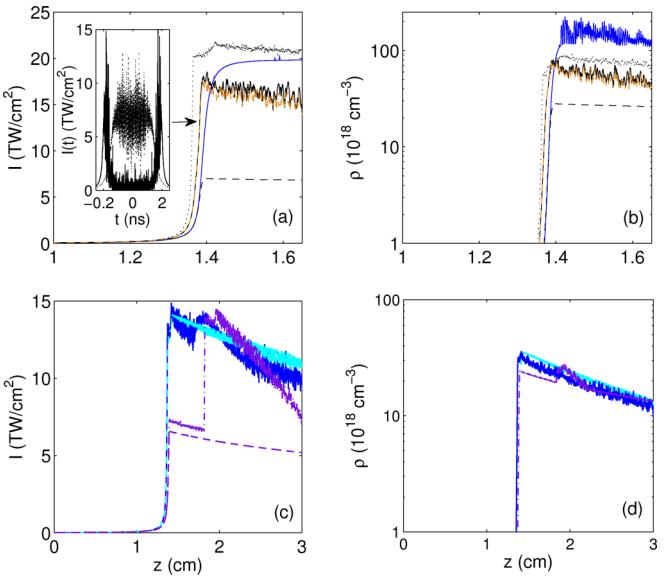

FIG. 3. (Color online) (a) Maximum intensity along z for the 60-μm, 0.77-ns pulse with 2 GHz phase modulation (blue [dark gray] curve) or when 1% amplitude random noise is introduced with (solid black curve) and without (dotted black curve) GVD [$k'' = 1169$ fs^2/cm] and TOD [$k''' = 348$ fs^3/cm], and with neither phase modulation nor noise seed (black dashed curve). The brown [light gray] dashed curve includes self-steepening effects. Inset details the temporal evolution of the maximum pulse intensity with 1% input random noise at $z = 1.39$ cm (dashed curve) and $z = 1.43$ cm (solid curve). (b) Corresponding peak electron densities, computed from the FME model. (c) Maximum intensity reached by the same pulse from the SBS-3D code and initially perturbed by a 5×10^{-4} random noise with an inertial plasma (violet dash-dotted curve), with a stationary plasma (violet dashed curve), 1% random noise (dark blue [dark gray] curve) and by a cosine perturbation lined up on the most unstable frequency $\Omega = 4.2 \times 10^4$ ns^{-1} with 1% amplitude (bright blue [light gray] curve). (d) Corresponding peak densities with same plot styles.

to Kerr-induced four-wave mixing. The blueshifted variation is linked to temporal scales of $\sim 2\pi/\Delta\omega \simeq 190$ fs, close to $\tau_{\rm rec}$. Note that the associated pulse intensity may be longer, with, e.g., a FWHM of 800 fs [see Fig. 2(c)], if the optical field acquires a chirped phase.

The previous results suggest that physical pulses undergoing small perturbations should rapidly turn to an ultrashort dynamic. To verify this assessment, Fig. 3 compares our reference pulse with the same pulse in which 1% random noise has been introduced into the input temporal amplitude. This noise seeds small-scale instabilities, which drive the nanosecond pulse to an ultrashort propagation regime when plasma generation sets in [see inset of Fig. 3(a)]. Once this transition is achieved, the pulse becomes shorter and shorter, so that we may wonder whether chromatic dispersion and pulse steepening can significantly affect the propagation. When including these higher-order effects, Fig. 3(a) shows that chromatic dispersion contributes to lower the clamping intensity, while space-time focusing and self-steepening remain negligible. Over the short propagation ranges examined here, both chromatic dispersion and pulse steepening do not severely modify the pulse dynamic. Figures 3(c) and 3(d) retrieve the previous tendencies when using the SBS-3D code. Here, very small perturbations (5×10^{-4} in amplitude), as well as moderately small perturbations (1% in amplitude) driven either by a random noise or by cosine modulations in the form $U_1(z = 0) \times [1 + 0.01 \cos(\Omega t)]$ with $\Omega = 2\pi/150$ fs^{-1}, break the quasistationary stage and force the pulse to enter an ultrafast dynamic characterized by the emergence of intense, picosecond subpulses [see, e.g., Figs. 4(c) and 4(d)]. Importantly, Figs. 3(c) and 4(b) reveal that the pulse remains insensitive to the small perturbations with a stationary plasma, which confirms the key role of the inertial nature of Eq. (13). Furthermore, Figs. 3(a) and 3(b) show the self-focusing of pump pulses being phase modulated, as further studied in Sec. V. One can see that such modulations also force the pump pulse to enter an ultrafast regime. Hence, when a potential source of disturbance (random noise, cosine or phase modulation) is introduced, we can expect a quasi-immediate destabilization of the nanosecond pulse into an ultrashort pulse dynamic.

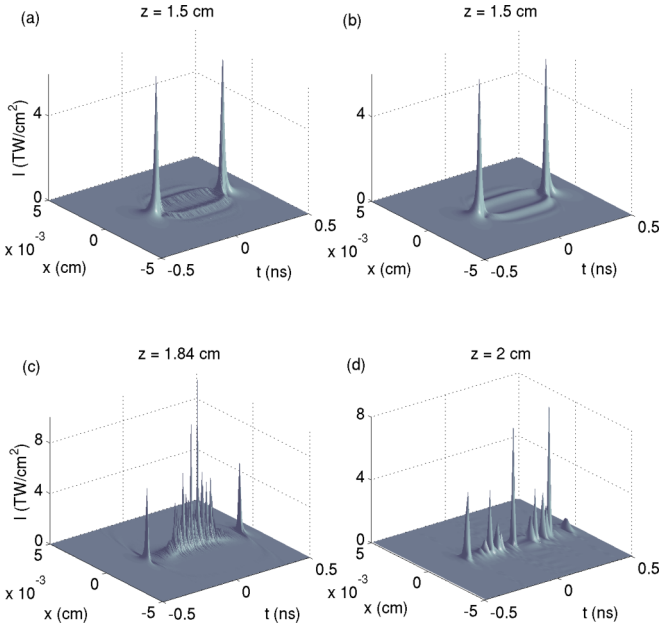

FIG. 4. (Color online) (x,t) intensity profiles (maximum along y) of the pulse shown in Figs. 3(c) and 3(d), computed from the SBS-3D code. Intensity profiles for (a) an inertial plasma and (b) a stationary plasma produced by a perturbed beam with 5×10^{-4} amplitude random noise at $z = 1.5$ cm. (c) Pulse instability along time with the inertial plasma at $z = 1.84$ cm. (d) Same at $z = 2$ cm with a cosine perturbation using $\Omega = 4.2 \times 10^4$ ns^{-1}.

IV. TWO-WAVES DYNAMICS

We now turn to the coupling of the pump and Stokes waves by switching on the Brillouin term ($g_0 \neq 0$) and henceforth employ the SBS-3D code. We consider nanosecond pump beams with initial width $w_0 = 15\ \mu$m and $w_0 = 60\ \mu$m. Their input intensities take the values $I_1(0) = 213$ GW/cm^2 [$P_1(0) = 2P_{\rm cr}$] and $I_1(0) = 26.7$ GW/cm^2 [$P_1(0) = 4P_{\rm cr}$], respectively. Maximum sample thickness is $L = 2.5$ cm, shortening the time step to $\Delta t \leqslant 7.5$ fs.

Figure 5 shows maximum intensities [Figs. 5(a) and 5(c)] and electron densities [Figs. 5(b) and 5(d)] for these two pulses. In Fig. 5(a), we can observe the strong increase of the 15-μm pump (solid dark blue curve) that occurs near the entrance face of the sample. This premature growth is absent for a stationary plasma (dashed bright blue curves). In Fig. 5(b), the inertial electron density follows the pump behavior. This rapidly increases at short propagation distances due to strong Stokes wave amplification near the entrance face. From $z > 0.1$ cm, the pump pulse enters an ultrashort propagation regime characterized by high clamped intensities (see previous section). The 60-μm pump repeats a similar dynamic over longer propagation distances [Fig. 5(c)]. It rapidly increases to several TW/cm^2 intensity levels over short distances before the "regular" collapse event amplifies the pulse intensity to even higher values. Figure 5(d) suggests a destabilizing action due to strong backscattering near the front face. A direct comparison with simulations imposing a stationary plasma shows that this early pump growth is linked to the temporal variations of the plasma response. In the trailing region of the pulse, sharp spikes can reach high intensity, but they are confined inside such a narrow time interval that the electron density cannot reach its highest peak value. This explains why, far after focus, the peak density sometimes decreases, whereas the peak intensity may go on increasing. Interestingly, we can observe the relaxation stage of the pump pulse, which seems partly attracted to a quasistationary regime in the range $1.4 \leqslant z \leqslant 1.7$ cm [see Fig. 5(c)]. Figure 6 details the spatiotemporal intensity profiles of the same pulses at a few distances close to and beyond the entrance window of the sample. With a stationary plasma, we refind the classical SBS-filamentation scenario [16], following which the pump self-focuses and transfers part of its power from the front to the rear zone, where the Stokes wave grows up (not shown). With a dynamical plasma, the pump increases earlier, well before the self-focusing distance. Near the dominant leading peak, narrow satellite spikes emerge over ~ps time scales and the optical components reach higher intensity values.

A. Plasma instabilities

Similarly to the one-wave case, the inertial nature of the plasma nonlinearity contributes to the above instabilities. Let us indeed consider Eqs. (10)–(13), where, for technical convenience, we omit the infinitesimally small thermal noise ($\tilde{N} \to 0$), and discard MPA losses and SBS phonon coupling. We assume a regime with two permanently created counterpropagating waves that preserve each their own partial power. The zeroth-order solution is then defined by the two stationary envelopes $U_{is} \equiv \phi_i e^{i\Lambda_i z}$, with $i = 1,2$ for the pump and Stokes waves, such that

$$\Lambda_1 = \frac{n_2\omega_0}{c}(I_{1s} + 2I_{2s}) - \alpha\left(I_{1s}^K + I_{2s}^K\right), \tag{31}$$

$$-\Lambda_2 = \frac{n_2\omega_0}{c}(I_{2s} + 2I_{1s}) - \alpha\left(I_{1s}^K + I_{2s}^K\right), \tag{32}$$

where α has been defined in Eq. (24) ($I_{is} \equiv |\phi_i|^2$). These plane-wave solutions are coupled to the stationary plasma density

$$\rho_s = \tau_{\rm rec}\sigma_K\rho_{\rm nt}\left(I_{1s}^K + I_{2s}^K\right), \tag{33}$$

whose perturbed state is again given by Eq. (26) with ρ_s including now the forward and backward plane waves. The perturbed optical states read as

$$U_i(\vec{r}_\perp,z,t) = U_{is}(\vec{r}_\perp,z) + \tilde{u}_i^+(\vec{r}_\perp,z)e^{-i\Omega t} + \tilde{u}_i^-(\vec{r}_\perp,z)e^{i\Omega t}, \tag{34}$$

with $\Omega = \bar{\Omega}$ and $|\tilde{u}_i^+,\tilde{u}_i^-| \ll |U_{is}|$. Straightforward linearization of Eq. (13) thus yields

$$\rho^+ = \bar{\rho}^- = K\rho_{\rm nt}\sigma_K \sum_{i=1,2} I_{is}^{K-1}\frac{(\tilde{u}_i^+\bar{U}_{is} + \bar{\tilde{u}}_i^- U_{is})}{\tau_{\rm rec}^{-1} - i\Omega}. \tag{35}$$

Inserting the above perturbed states into Eqs. (10)–(13) with $(g_0, Q) \to 0$, we are left with coupled equations for $\tilde{u}_i^\pm = u_i^\pm e^{i\Lambda_i z}$, $i = 1,2$. We combine the resulting linearized

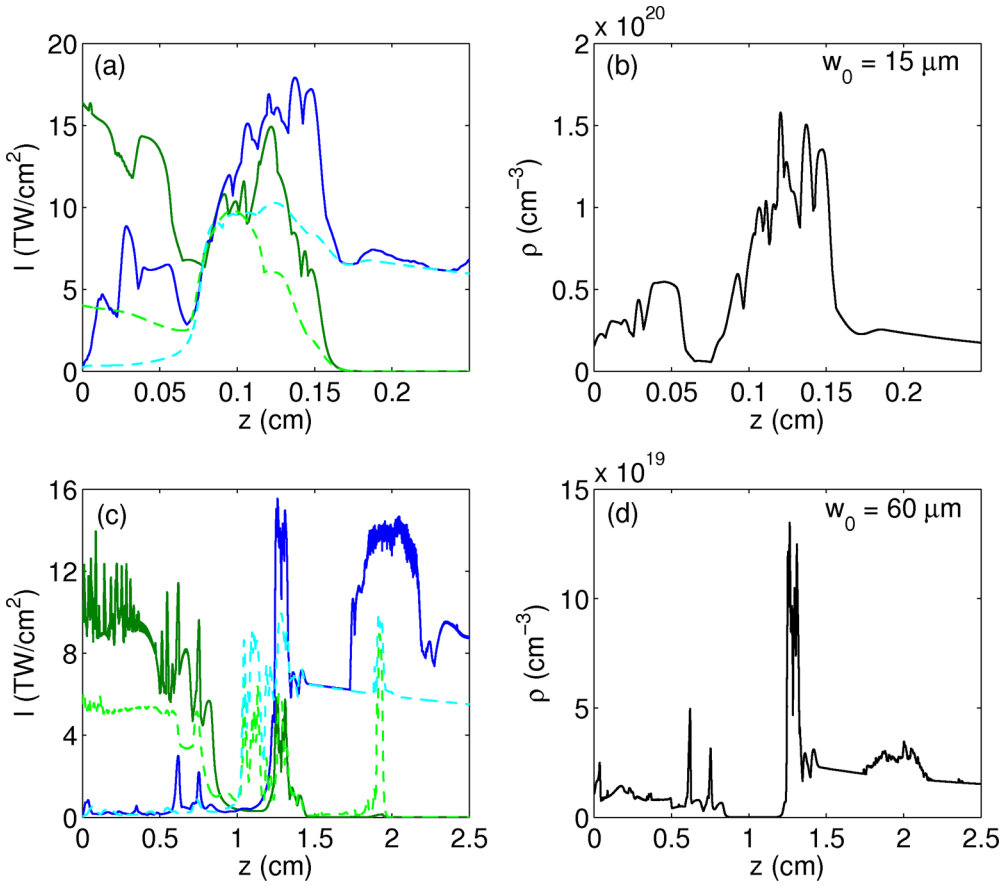

FIG. 5. (Color online) (a) Peak intensity and (b) electron density along z for the 355-nm pulse with $w_0 = 15$ μm. Blue (dark gray) curves refer to the forward pump; green (light gray) curves refer to the backward Stokes pulse. Dark solid curves correspond to a dynamical plasma response, whereas the bright dashed ones refer to a stationary plasma ($\partial_t \rho = 0$). In (b),(d), the black curves illustrate the electron density computed with a dynamical plasma. (c),(d) Same quantities as in (a),(b), but for the broader beam width $w_0 = 60$ μm.

equations for the new perturbative eigenstates $v_i = u_i^+ + \bar{u}_i^-$ and $w_i = u_i^+ - \bar{u}_i^-$, that oscillate with the transverse wave

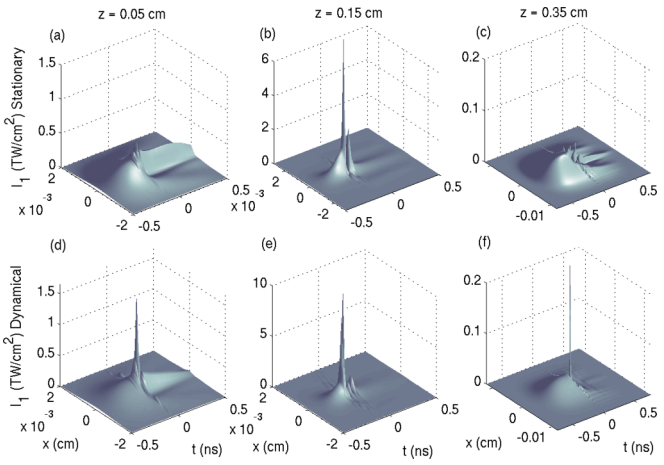

FIG. 6. (Color online) Pump (x,t) intensity profiles for $w_0 = 15$ μm at $z = 0.05$ cm and $z = 0.15$ cm: (a),(b) refer to a stationary plasma; (d),(e) involve a dynamical plasma response. Graphical resolution is 7.2 ps. (c),(f) Same quantities for the pulse with $w_0 = 60$ μm at $z = 0.35$ cm; (c) stationary plasma; (f) dynamical plasma. Graphical resolution is 7.5 ps. This explains why the maximum intensities of Fig. 5 cannot be attained.

vector $\vec{k}_\perp$ and are found to obey

$$[\pm\partial_z - ik'\Omega]v_i = -i\frac{k_\perp^2}{2k_0}w_i, \tag{36}$$

$$[\pm\partial_z - ik'\Omega]w_i = i\left[2\left(\frac{n_2\omega_0}{c}I_{is} - \frac{\alpha K I_{is}^K}{1 - i\Omega\tau_{\rm rec}}\right) - \frac{k_\perp^2}{2k_0}\right]v_i + i\sqrt{I_{is}I_{js}}\left[\frac{4n_2\omega_0}{c} - \frac{2\alpha K I_{js}^{K-1}}{1 - i\Omega\tau_{\rm rec}}\right]v_j, \tag{37}$$

where $i \neq j = 1,2$; $+$ and $-$ signs apply to the forward and backward waves, respectively. Looking for perturbations growing as $\sim e^{\lambda z}$, the growth rate is given by

$$\lambda_+ = {\rm Re}\left[\frac{k_\perp}{\sqrt{2k_0}}\sqrt{2\Delta_+ - \frac{k_\perp^2}{2k_0}}\right], \tag{38}$$

where

$$2\Delta_\pm = \frac{n_2\omega_0}{c}(I_{1s} + I_{2s}) - \alpha K\frac{I_{1s}^K + I_{2s}^K}{1 - i\Omega\tau_{\rm rec}} \pm\left\{\left[\frac{n_2\omega_0}{c}(I_{1s} - I_{2s}) - \alpha K\frac{I_{1s}^K - I_{2s}^K}{1 - i\Omega\tau_{\rm rec}}\right]^2\right.$$

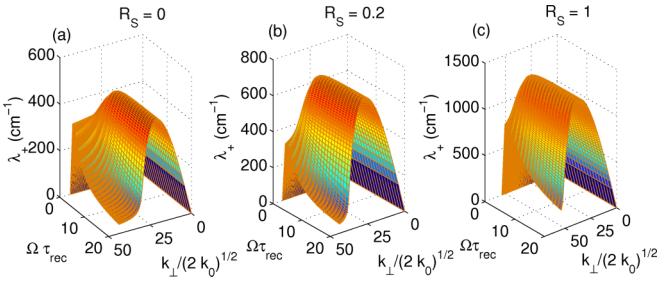

FIG. 7. (Color online) Contour plots of the growth rate λ_+ [cm^{-1}] in the plane $(k_\perp/\sqrt{2k_0},\Omega\tau_{\rm rec})$ for $\lambda_0 = 355$ nm, $w_0 = 60\ \mu$m, and pump stationary intensity $I_{1s} \equiv I_0 = 7$ TW/cm^2. $R_S = I_{2s}/I_{1s}$ denotes the stationary Stokes-pump intensity ratio. (a) $R_S = 0$, (b) $R_S = 0.2$, and (c) $R_S = 1$.

$$+4I_{1s}I_{2s}\left(\frac{2n_2\omega_0}{c}-\frac{\alpha K I_{1s}^{K-1}}{1-i\Omega\tau_{\rm rec}}\right)$$

$$\times\left(\frac{2n_2\omega_0}{c}-\frac{\alpha K I_{2s}^{K-1}}{1-i\Omega\tau_{\rm rec}}\right)\Bigg\}^{1/2}. \qquad (39)$$

Equation (38) is stated under the limit $k'\Omega \to 0$, as linear dispersion does not directly contribute to instability. We can notice that such a growth rate is similar to that earlier derived by Luther and McKinstrie for a purely Kerr medium [55], i.e., in the limit $\Omega \to +\infty$.

Figures 7(a)–7(c) illustrate some growth rates in the $(\Omega, k_\perp)$ plane. When the pump-Stokes intensity ratio $R_s = I_{2s}/I_{1s}$ is increased, the modulational instability growth rate λ_+ increases. We refind the major characteristics of the inertial plasma instability, i.e., the growth rate is everywhere positive except for $\Omega = 0$, where plane waves are stable (stationary plasma regime). Unstable modes with maximum growth rate occur with a frequency located around $\Omega\tau_{\rm rec} = 1$, signaling plasma destabilization of the pump wave over the free electron lifetime. This plasma-driven instability is responsible for the pump growth at early propagation distances in Figs. 5(a) and 5(c).

V. PHASE MODULATIONS

A current technique for inhibiting Brillouin backscattering is to employ broadband pump pulses with rapid phase fluctuations [2,14,15,22,24] chosen in the form

$$U_1(z=0) = \sqrt{I_1(0)}\, e^{-(x^2+y^2)/w_0^2 - t^{2N}/t_p^{2N} + im\sin(2\pi\nu_m t)}. \qquad (40)$$

Here, the modulation depth $m \gg 1$ and the modulation frequency ν_m produce a wide enough $1/e$ spectral bandwidth $\Delta\nu \simeq 2m\nu_m$ in the pump, whose spectrum is then composed of $\sim 2m$ modes [16]. When these modes are spaced by $\nu_m > \Delta\nu_B = \Gamma_B/2\pi$ and for small enough coherence length, each pump mode scatters its own Stokes pulse with no interaction between their neighbors [14,23,24]. For pump modes of equal initial intensity $\sim I_1(0)/2m$, the exponential Brillouin gain G_T is then decreased significantly compared to an unmodulated pump.

Let us here recall that phase modulations with moderate pump bandwidth (<100 GHz) are less efficient for collapsing waves [15]. In this configuration indeed, the pump, being strongly focused by the Kerr nonlinearities, can undergo temporal and spatial short-scale instabilities and thus self-focus at much shorter propagation distances [16]. To avoid such instabilities, selecting a broad enough pump bandwidth is necessary. By working out on the energy exchanges between pump and Stokes waves, preventing the growth of Stokes modes demands at least that the pump bandwidth $\Delta\nu$ satisfies

$$\Delta\nu \gg \Delta\nu_{\rm cr} = \tfrac{1}{4}\Gamma_B g_0 I_1(0) L. \qquad (41)$$

In addition, the modulation depth m must be chosen in such a way that the gain does not reach the minimum Brillouin threshold $G_{\rm TH} \approx 25$–30 [10,11].

In Fig. 8, phase modulation has been used with $m = 21$ to suppress SBS for the 60-μm pump pulse with $I_1(0) = 26.7$ GW/cm^2. As expected, the larger the pump bandwidth, the lesser the pump depletion. Figures 8(a)–8(c) show the power profiles corresponding to the input pump (black curves), to the laser pulse exiting the 2.5-cm-thick sample (blue curves), and to the Stokes wave reflected at $z = 0$ (green curves). Input phase modulations develop amplitude fluctuations once the pump has been advanced in time to about half its FWHM duration. From Ref. [16] and the approximate estimate (41), initial intensities of about 30 GW/cm^2 still suffer Brillouin scattering with a modulation frequency as low as $\nu_m = 2$ GHz. Instead, broad bandwidths of $\approx$1000 GHz are requested for this intensity level at 355 nm, which invites us to choose $\nu_m > 23.8$ GHz. Using $\nu_m = 30$ GHz [Figs. 8(c) and 8(f)], it is indeed observed that a large enough modulation frequency removes SBS. From Figs. 8(d)–8(f) the pump energy is depleted for $\nu_m = 0$ and 2 GHz, i.e., as long as Brillouin scattering remains

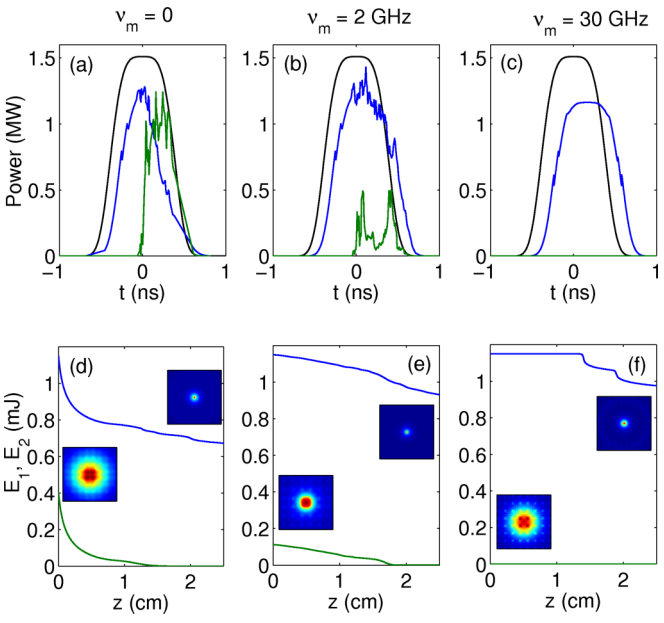

FIG. 8. (Color online) Power profiles for input (black curves), transmitted pump (blue [dark gray] curves), and reflected Stokes (green [light gray] curves) pulses for $w_0 = 60\ \mu$m: (a) without phase modulation, (b) with $\nu_m = 2$ GHz, and (c) $\nu_m = 30$ GHz ($m = 21$). (d)–(f) Corresponding partial energy decreases with same color plot styles. Insets detail Stokes and pump fluences in the (x, y) plane at $z = 0$ and $z = 2.5$ cm, respectively. Transverse surfaces are 50 μm $\times$ 50 μm.

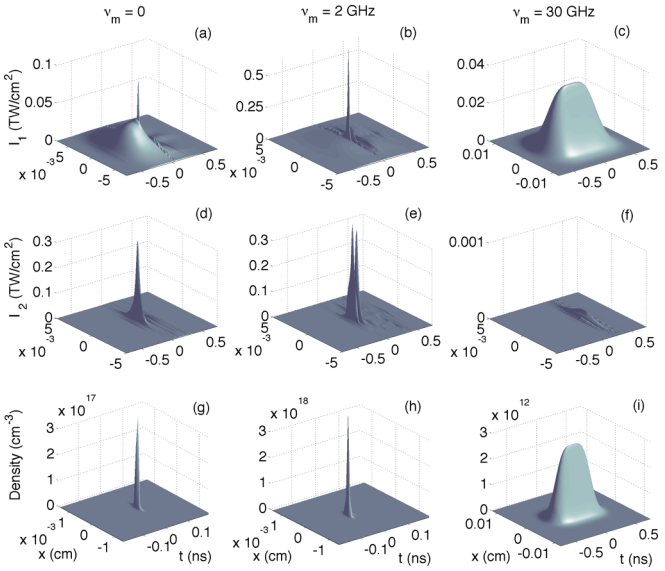

FIG. 9. (Color online) (a)–(c) 60-μm pump intensity profiles in the (x,t) plane, (d)–(f) associated Stokes waves, and (g)–(i) plasma densities for $\nu_m = 0$ (left column), $\nu_m = 2$ GHz (middle), and $\nu_m = 30$ GHz (right column). The selected propagation distance is $z = 0.5$ cm. Input beam parameters are $w_0 = 60$ μm, $\lambda_0 = 355$ nm, and $I_1(0) = 26.7$ GW/cm^2. Graphical resolution is limited to 7.5 ps.

active. When the latter is suppressed with $\nu_m = 30$ GHz, only MPA losses are retrieved from the pump self-focusing distance. Direct measurements of backscattered fluences, $F_2 \equiv \int I_2(0,t)dt$, yield the value $F_2 \simeq 12$ mJ/cm^2 with $\nu_m = 0$, down to $F_2 \simeq 1.14$ μJ/cm^2 with $\nu_m = 30$ GHz. These show a net decrease of the Stokes fluence that remains below the damage thresholds expected at 355 nm ($F_{\rm th} \sim 12$–14 J/cm^2).

When SBS is efficiently suppressed, plasma generation should cease near the entrance face and, thereby, the modulational instabilities amplifying the pump should disappear too. This is confirmed by Fig. 9, that details the spatial and temporal distributions of the pump and Stokes intensities together with the electron density for the modulation frequencies $\nu_m = 0$, 2 GHz and 30 GHz at $z = 0.5$ cm. With $\nu_m = 0$, the pump wave is amplified near the front face of the material, because strong backscattering dramatically augments the plasma response, which induces temporal instabilities by feedback. With $\nu_m = 2$ GHz, this instability is even reinforced by ~ps-long peaks breaking the pump distribution along time. With $\nu_m = 30$ GHz, all instabilities disappear. SBS is negligible at the entrance face, so that the plasma response is limited to small values and the pump profile remains preserved.

VI. INFRARED PUMP

In this section, we examine pulses operating at 1.064 μm central wavelength, i.e., the fundamental of the former 3ω wavelength. We still choose a reference pump pulse defined by a 60-μm transverse Gaussian profile and a 0.77-ns (FWHM) super-Gaussian profile in time. Simulations are performed by means of the SBS-3D code with the waived transverse resolution of $\Delta x = \Delta y = 1.87$ μm, as the filament size is expected to increase linearly with λ_0 [56]. Longitudinal and time increments are $\Delta z \leqslant 1.5$ μm and $\Delta t \leqslant 7.4$ fs.

Let us first comment on pulse propagation with no phase modulation. Accessing input powers close to four critical powers requires intensities as high as $I_0 = 302$ GW/cm^2 (see Table I). Compared with our former UV pulse, the collapse distance is shortened by a factor of ~3, due to the proportional decrease of the Rayleigh length. Moreover, using Eq. (17), when plasma defocusing takes place over 1 ps time interval, the clamping intensity increases to $I_{\rm max} \simeq 8.83$ TW/cm^2 in the IR. When plasma is active over the recombination time $\Delta\tau = 150$ fs, $I_{\rm max}$ is augmented to $I_{\rm max} = 11.6$ TW/cm^2 at 1.064 μm. Hence higher intensities are necessary to trigger plasma generation at long wavelengths and so should be the energy losses.

Figures 10(a) and 10(b) confirm these features, by showing the peak intensity of a single pulse with no Brillouin effect (solid curve), the pump energy dissipation due to MPA (dashed curve), and associated free electron density. The first observation is the higher clamping intensity reaching about 11 TW/cm^2 within a first stage ($z < 1.3$ cm), that resembles the nanosecondlike clamping intensity scheme. The second feature is the later growth of the beam intensity up to 16 TW/cm^2, which may signal an instability driving the nanosecond pulse to an ultrashort dynamic. The peak plasma density only reaches $\sim 8 \times 10^{18}$ cm^{-3} [Fig. 10(b)]. These behaviors are representative of ionization at long carrier wavelength, which is more difficult to achieve than in the UV (8 IR photons against 3 UV photons).

Figure 10(c) details the two-peaked structure characterizing the quasistationary interplay between multiphoton ionization and self-focusing for a single wave. This structure forms a second, thinner parabola in the (z,t) plane when $z = 1$ cm [Fig. 10(d)]. At $z \simeq 1.5$ cm, the pulse profile decays into multiple, short temporal peaks associated with an ultrashort pulse dynamic and plasma-driven instability [Fig. 10(e)]. Evaluation of the filament diameter is $\phi_p \simeq 7.5$ μm, being three times the UV filament diameter, as expected.

Figures 10(a) and 10(b) also display the self-focusing of another isolated pump wave with weaker initial intensity of 162 GW/cm^2 ($P_{\rm in} = 2P_{\rm cr}$) and related plasma response. Here, the local numerical noise and input intensity are not sufficient to trigger short-time instabilities.

We employ the latter beam configuration to examine the effect of Brillouin scattering over 2 cm of fused silica. Introducing $g_0 \neq 0$ causes an efficient backscattering over the sample thickness $L = 2$ cm (Fig. 11). Again, an early instability leads to a premature amplification of the pump pulse [Fig. 11(c)]. A stationary plasma, in contrast, regularizes this early stage of propagation and better preserves the pump distribution [see Fig. 11(d) whose Stokes component is displayed in Fig. 11(e)]. Plasma instabilities develop near the entrance face of the silica window, which forces the pump beam to diverge at short propagation distances. Even at small density levels [$< 10^{17}$ cm^{-3}, see inset of Fig. 11(b)], we checked that in the longitudinal range $z < 0.5$ cm, unstable modes triggered by a dynamical plasma can develop with relevant growth rate $\lambda_+ \sim 0.1$ cm^{-1} whenever the pump intensity is of the order of 1 TW/cm^2 while R_S exceeds unity (e.g., $R_S = 5$).

Figures 12(a) and 12(b) show the power profile of the initial pump, the exiting power, and the backscattered power through

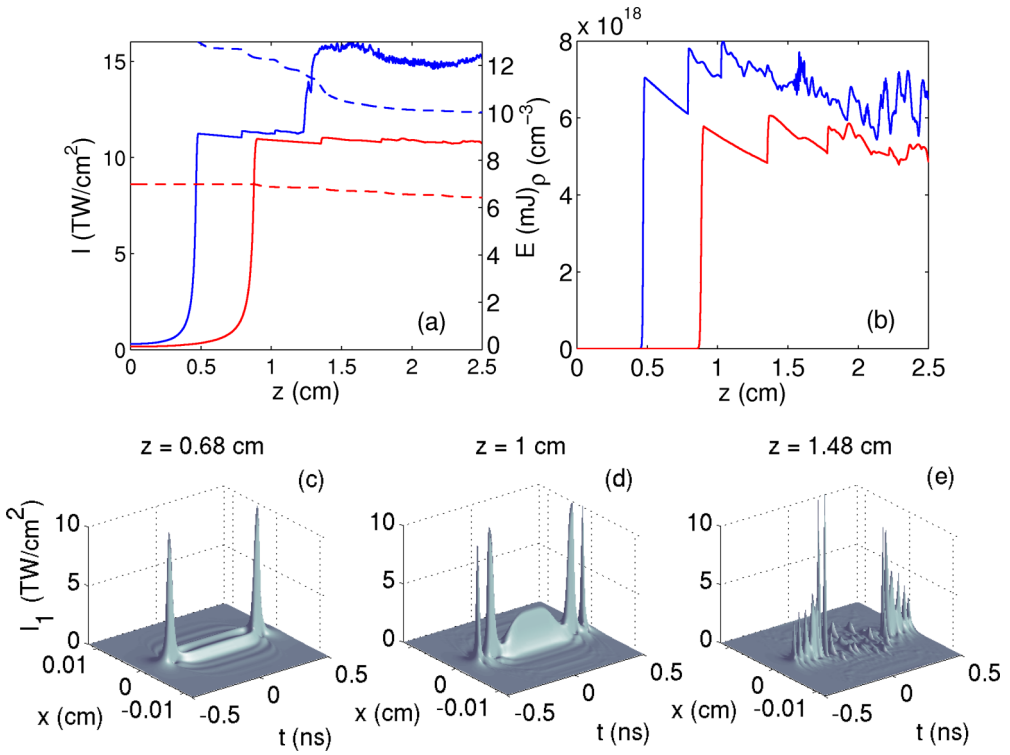

FIG. 10. (Color online) (a) Peak intensity (left axis, solid curve) and energy variations (right axis, dashed curve) of a single ($g_0 = 0$), infrared Gaussian pulse with 60-μm beam width and 0.77 ns FWHM duration self-focusing in silica with $I_0 = 302$ GW/cm^2 (blue [dark gray] curves) and $I_0 = 162$ GW/cm^2 (red [light gray] curves). (b) Corresponding plasma densities. (c)–(e) (x,t) intensity profiles of the single pulse with $I_0 = 302$ GW/cm^2 at various distances showing the two peaks resulting from early defocusing in the nanosecond propagation regime (primary parabola), the formation of secondary parabola, and their decay into picosecond peaks (instability).

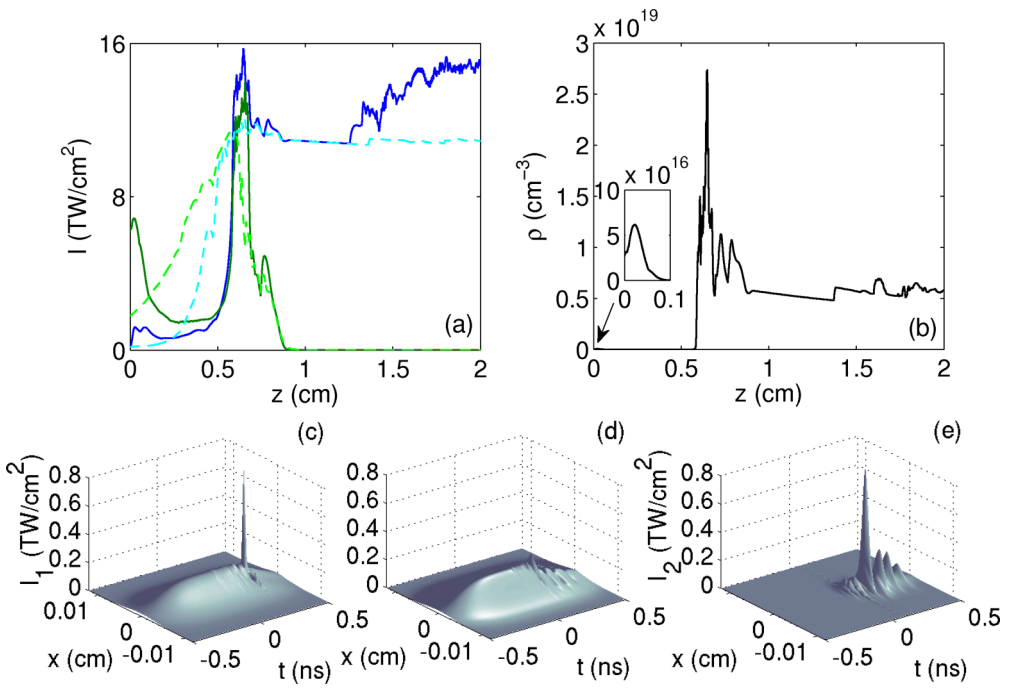

FIG. 11. (Color online) (a) Peak intensity of an infrared pump pulse with 60-μm beam width and 0.77 ns FWHM duration self-focusing with Brillouin effect ($I_0 = 162$ GW/cm^2) over $L = 2$ cm. The solid dark (dynamical plasma) and dashed bright (stationary plasma) blue (dark gray) curves refer to the pump pulse; the green (light gray) curves refer to the Stokes wave. (b) Corresponding plasma density; inset zooms short propagation distances. (c)–(e) (x,t) intensity profiles of pump pulses (c) with and (d) without a dynamical plasma response at $z = 0.12$ cm; (e) shows the Stokes intensity corresponding to the latter regime. Graphical resolution is ~6 ps.

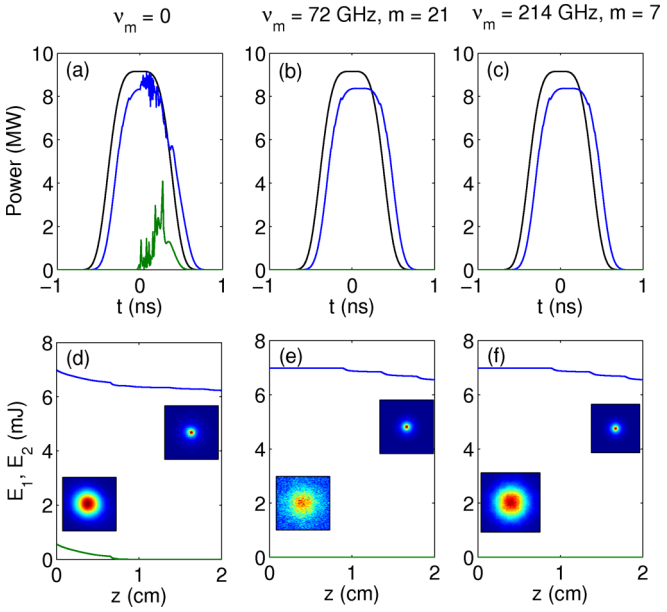

FIG. 12. (Color online) Power distributions of an infrared pulse with 60-μm beam width, $I_0 = 162$ GW/cm^2 (a) without and with phase modulation driven by (b) $\nu_m = 72$ GHz and $m = 21$, and (c) $\nu_m = 214$ GHz and $m = 7$. The black curve is the power entering a 2-cm-thick silica sample; the blue (dark gray) curve is the power exiting the sample and the green (light gray) curve is the Stokes power at the entrance of the sample. (d)–(f) Partial energy variations (d) without and (e),(f) with phase modulations. Insets show (x,y) fluence profiles of the pump at $z = 2$ cm and of the Stokes wave at $z = 0$. Transverse surfaces are 50 μm $\times$ 50 μm.

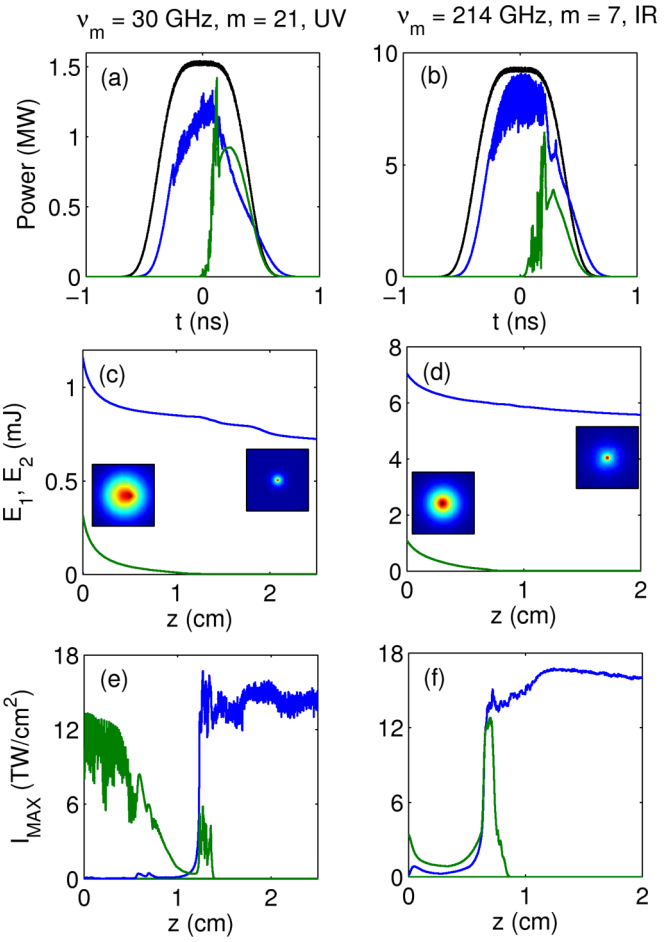

FIG. 13. (Color online) (a),(b) Power distributions of the UV and IR pulses used in (a) Fig. 8 and (b) Fig. 12, but for a pump pulse affected by 1% amplitude random noise. (c),(d) Partial energies and fluence patterns. Transverse surfaces are 50 μm $\times$ 50 μm in the (x,y) plane. (e),(f) Peak intensities of the pump (blue [dark gray] solid curves) and Stokes pulse (green [light gray] solid curves).

2 cm of silica for the $2P_{cr}$ pump pulse undergoing phase modulations. On the basis of Ref. [16], a total bandwidth of about 3000 GHz is needed to suppress SBS at 1064 nm for input intensity levels $\sim$160 GW/cm^2. So, using a modulation depth $m = 21$, a modulation frequency $\nu_m = 72$ GHz should be in principle sufficient. Additionally, we tested a lesser number of modes, choosing $m = 7$, and higher modulation frequency of 214 GHz. With these values, Figs. 12(b) and 12(c) display evidence that again in the IR domain backscattering can be totally suppressed by appropriate phase modulations. In Figs. 12(d)–12(f), the fluence patterns shown as insets reveal a reflected fluence of 25 mJ/cm^2 without phase modulation and below 10^{-7} mJ/cm^2 with phase modulation. When a broad enough bandwidth is employed, the scenario of a single-wave collapse is retrieved.

VII. ROBUSTNESS OF PHASE MODULATIONS VERSUS RANDOM NOISE

A remaining issue is to evaluate the robustness of the previous phase modulations to keep the Stokes wave at negligible levels in the presence of amplitude fluctuations in the pump pulse. Such fluctuations may be induced by some local noise in the laser source or by smoothing techniques delivering speckle patterns that affect stochastically the averaged intensity of the pump. One can thus wonder whether such disturbances in the pump may alter the efficiency of phase modulations. To clear up this issue, we repeated the simulation employing a 355-nm, phase-modulated pump pulse with 30-GHz frequency modulation and $m = 21$ modulation depth, but being initially affected by a 1% amplitude random noise. We did the same for the 1.064 μm pump pulse with $\nu_m = 214$ GHz and $m = 7$.

Figure 13 shows the power profiles of the pump and Stokes pulse under the previous conditions. We clearly see the reemergence of a Stokes component, simply due to the initial noise in the pump for both laser wavelengths. It is important to notice that the backscattered fluence is now able to reach $\sim$12 J/cm^2 at 355 nm (0.6 J/cm^2 at 1.064 μm), thus approaching damage thresholds. The same information can be inferred from the individual pulse energies as the pump reloses an important fraction of energy due to an efficient Brillouin effect. In terms of intensities, Figs. 13(e) and 13(f) display evidence of the reappearance of strong backscattering accompanied by early instabilities that shift the nonlinear focus backward upon the propagation axis and enhance the level of clamping intensities. This applies to initially perturbed UV pulses as well as to perturbed IR pulses. Hence initial fluctuations in the pump, even at weak amplitude levels, are able to break the efficiency of phase modulations at nonlinear focus, trigger instabilities earlier over the

propagation axis, and backscatter an important amount of Stokes intensity.

Our results complete those published in Refs. [15,16], where phase modulations were applied on clean, i.e., unperturbed, pulses. In [15], 100 GHz bandwidths were shown to produce modulational instabilities shortening the self-focusing distance of the pump and amplifying backscattered components. In [16], an efficient suppression of SBS was achieved by using broader bandwidths. Here, we focused on the action of dynamical ionization. We demonstrated that, with active SBS, an inertial plasma source can also destabilize self-focusing pump and Stokes waves when the ionization threshold is reached. This plasma-driven instability is linked to the change in the refractive index caused by the backscattered wave and, therefore, it can be turned off at early propagation distances by appropriate phase modulations. However, this technique may be fragile during the damage creation process when the latter is induced by noisy laser pulses.

VIII. CONCLUSION

In summary, we have numerically investigated the coupling between Kerr-self-focusing, stimulated Brillouin scattering, and plasma generation driven by nanosecond pulses in fused silica. We examined the effect of a dynamical ionization on the pump and Stokes waves self-focusing inside the bulk material at ultraviolet and infrared wavelengths. The plasma response here consists of multiphoton ionization saturated by electron recombination. We reported the occurrence of plasma-driven modulational instabilities which emerge when the input pulses are not necessarily subject to external perturbations, after a regime of quasistationary interplay between Kerr focusing and multiphoton ionization. The instability stage has been modeled through a plane-wave stability analysis [21], revealing the existence of unstable temporal modes whose optimal frequency is close to the inverse of the electron recombination time. Confirmed numerically, such instabilities develop from the Kerr compression of the pulse along the self-focusing stage. They originate from the finite lifetime of the plasma over which the most compressed part of initially long pulses tends to be broken in. This instability favors the production of more ultrashort peaks in the wave profile. Thereby, the nanosecond pulse dynamic transforms itself into a femtosecond one. In the presence of small temporal fluctuations, the quasistationary stage disappears and the pulse enters an ultrashort filamentation regime during its first self-focusing stage.

By switching on the Brillouin effect, we measured strong backscattering when letting unperturbed Gaussian pulses propagate over a few cm of silica. Because of the temporal perturbations induced by acoustic waves and scattering process, a self-focusing pulse undergoes an ultrashort dynamic without the need of external noise. The main difference with the single-wave configuration is that plasma-driven instabilities already occur at short distances, since they are also excited by the Stokes waves which attain a high intensity at the entrance face of the sample. By simple feedback, the pump wave gets destabilized and reaches in turn high intensity levels at short propagation distances. The existence of such plasma-driven instabilities occurring over electron recombination times has been justified by a two-plane-wave stability analysis.

To get rid of these sources of damage, phase modulations usually provide efficient tools breaking the pump into a train of picosecond subpulses along which acoustic waves have no time to be excited. We here demonstrated that phase modulations can still significantly reduce the backscattered fluence level even with an inertial plasma response. High modulation depth combined with large enough modulation frequency can inhibit SBS. In that case, not only backscattering but also early plasma contributions vanish, which permits one to preserve the distribution of the pump pulse. However, we must keep in mind that weak fluctuations in the input broadband pump can alter the action of phase modulations by causing an enhancement of Brillouin backscattering, which should limit the efficiency of this smoothing technique.

In conclusion, this work provides a numerical investigation of coupled nanosecond pulses undergoing a dynamical plasma response. It shows that optically driven plasma generation contributes to enhance the level of potential instabilities when long pump pulses go across Kerr media. However, phase modulations can still remain an efficient means for suppressing not only SBS, but also plasma-induced instabilities, provided that they supply a broad enough bandwidth and are applied to clean enough laser pumps.

ACKNOWLEDGMENTS

The authors thank Stefan Skupin and Christian Köhler for their help in the numerical treatment of the plasma source equation and for fruitful discussion. This study was performed using High Performance Computing (HPC) resources of TGCC/CCRT. It was granted under the allocation 2013-x2013057027 made by GENCI (Grand Equipement National de Calcul Intensif).

[1] H. Bercegol, L. Lamaignère, V. Cavaro, and M. Loiseau, Proc. SPIE **5991**, 59911Z (2005).

[2] J. R. Murray, J. R. Smith, R. B. Ehrlich, D. T. Kyrazis, C. E. Thompson, T. L. Weiland, and R. B. Wilcox, J. Opt. Soc. Am. B **6**, 2402 (1989).

[3] E. P. Ippen and R. H. Stolen, Appl. Phys. Lett. **21**, 539 (1972).

[4] V. I. Kovalev and R. G. Harrison, Phys. Lett. A **374**, 2297 (2010).

[5] G. S. He, C. Lu, Q. Zheng, P. N. Prasad, P. Zerom, R. W. Boyd, and M. Samoc, Phys. Rev. A **71**, 063810 (2005).

[6] Z. Zhu, D. J. Gauthier, and R. W. Boyd, Science **318**, 1748 (2007).

[7] Y. Okawachi, M. S. Bigelow, J. E. Sharping, Z. Zhu, A. Schweinsberg, D. J. Gauthier, R. W. Boyd, and A. L. Gaeta, Phys. Rev. Lett. **94**, 153902 (2005).

[8] L. Ren and Y. Tomita, J. Opt. Soc. Am. B **26**, 1281 (2009).

[9] V. I. Kovalev, N. E. Kotova, and R. G. Harrison, Opt. Express **17**, 2826 (2009).
[10] R. W. Boyd, *Nonlinear Optics* (Academic Press, San Diego, 1992).
[11] G. P. Agrawal, *Nonlinear Fiber Optics*, 3rd ed. (Academic Press, San Diego, 2001).
[12] R. L. Carman, F. Shimizu, C. S. Wang, and N. Bloembergen, Phys. Rev. A **2**, 60 (1970).
[13] I. Bar-Joseph, A. A. Friesem, E. Lichtman, and R. G. Waarts, J. Opt. Soc. Am. B **2**, 1606 (1985).
[14] G. Arisholm and P. Narum, IEEE J. Quant. Electron. **28**, 2075 (1992).
[15] S. Mauger, L. Bergé, and S. Skupin, New J. Phys. **12**, 103049 (2010).
[16] S. Mauger, L. Bergé, and S. Skupin, Phys. Rev. A **83**, 063829 (2011).
[17] S. Mauger, L. Bergé, and S. Skupin, Phys. Rev. A **85**, 029902(E) (2012).
[18] J. Schwarz and J.-C. Diels, Phys. Rev. A **65**, 013806 (2001).
[19] A. Vinçotte and L. Bergé, Phys. Rev. A **70**, 061802(R) (2004).
[20] S. Mauger, G. Colin de Verdière, L. Bergé, and S. Skupin, J. Comput. Phys. **235**, 606 (2013).
[21] T. A. Niday, E. M. Wright, M. Kolesik, and J. V. Moloney, Phys. Rev. E **72**, 016618 (2005).
[22] G. C. Valley, IEEE J. Quant. Electron. **22**, 704 (1986).
[23] E. Lichtman, A. A. Friesem, R. G. Waarts, and H. H. Yaffe, J. Opt. Soc. Am. B **4**, 1397 (1987).
[24] Y. Aoki and K. Tajima, J. Opt. Soc. Am. B **5**, 358 (1988).
[25] R. W. Boyd, K. Rzazewski, and P. Narum, Phys. Rev. A **42**, 5514 (1990).
[26] S. Tzortzakis, L. Sudrie, M. Franco, B. Prade, A. Mysyrowicz, A. Couairon, and L. Bergé, Phys. Rev. Lett. **87**, 213902 (2001).
[27] J. R. Peñano, P. Sprangle, B. Hafizi, W. Manheimer, and A. Zigler, Phys. Rev. E **72**, 036412 (2005).
[28] P. K. Kennedy, IEEE J. Quant. Electron. **31**, 2241 (1995).
[29] E. Yablonovitch and N. Bloembergen, Phys. Rev. Lett. **29**, 907 (1972).
[30] M. D. Feit and J. A. Fleck, Appl. Phys. Lett. **24**, 169 (1974).
[31] L. V. Keldysh, Sov. Phys. JETP **20**, 1307 (1965).
[32] P. Audebert, P. Daguzan, A. Dos Santos, J.-C. Gauthier, J.-P. Geindre, S. Guizard, G. Hamoniaux, K. Krastev, P. Martin, G. Petite, and A. Antonetti, Phys. Rev. Lett. **73**, 1990 (1994).
[33] H. Li and K. Ogusu, Jpn. J. Appl. Phys. **38**, 6309 (1999).
[34] L. Bergé, Phys. Rep. **303**, 259 (1998).
[35] L. Bergé, Phys. Rev. E **58**, 6606 (1998).
[36] J. H. Marburger, Prog. Quantum Electron. **4**, 35 (1975).
[37] A. V. Husakou and J. Herrmann, Phys. Rev. Lett. **87**, 203901 (2001).
[38] L. Bergé, S. Skupin, R. Nuter, J. Kasparian, and J. P. Wolf, Rep. Prog. Phys. **70**, 1633 (2007).
[39] D. Anderson and M. Lisak, Phys. Rev. A **27**, 1393 (1983).
[40] L. Bergé and S. Skupin, Phys. Rev. E **71**, 065601(R) (2005).
[41] S. Skupin and L. Bergé, Physica D **220**, 14 (2006).
[42] L. Bergé, S. Mauger, and S. Skupin, Phys. Rev. A **81**, 013817 (2010).
[43] L. Bergé and J. J. Rasmussen, Phys. Plasmas **3**, 824 (1996).
[44] D. Anderson, M. Bonnedal, and M. Lisak, Phys. Fluids **22**, 1838 (1979).
[45] D. Anderson, Phys. Rev. A **27**, 3135 (1983).
[46] T. J. Alexander and L. Bergé, Phys. Rev. E **65**, 026611 (2002).
[47] L. Bergé and A. Couairon, Physica D **152-153**, 752 (2001).
[48] J. J. Rasmussen and K. Rypdal, Phys. Scr. **33**, 481 (1986).
[49] K. Rypdal and J. J. Rasmussen, Phys. Scr. **33**, 498 (1986).
[50] G. Fibich and G. Papanicolaou, SIAM J. Appl. Math. **60**, 183 (1999).
[51] A. Couairon and L. Bergé, Phys. Plasmas **7**, 193 (2000).
[52] V. I. Bespalov and V. I. Talanov, JETP Lett. **3**, 307 (1966).
[53] A. J. Campillo, S. L. Shapiro, and B. R. Suydam, Appl. Phys. Lett. **23**, 628 (1973).
[54] N. Akhmediev, A. Ankiewicz, J. M. Soto-Crespo, and J. M. Dudley, Phys. Lett. A **375**, 775 (2011).
[55] G. G. Luther and C. J. McKinstrie, J. Opt. Soc. Am. B **7**, 1125 (1990).
[56] L. Bergé, Opt. Express **16**, 21529 (2008).